Int. J. Heat Mass Transfer. Vol. 27, No. 10, pp. 1879–1891, 1984
Printed in Great Britain

0017 9310/84 $3.00 + 0.00

Natural convection in a porous layer heated and cooled along one vertical side

DIMOS POULIKAKOS
Mechanical Engineering Department, University of Illinois at Chicago, Box 4348, Chicago, IL 60680, U.S.A.

and

ADRIAN BEJAN
Mechanical Engineering Department, University of Colorado, Campus Box 427, Boulder, CO 80309, U.S.A.

(*Received* 31 *October* 1983 *and in revised form* 24 *January* 1984)

Abstract—This paper describes the heat transfer and fluid flow through a confined porous layer heated and cooled along one of the vertical side walls. In the first part of the study, consideration is given to the case when the side-heating effect is positioned above the side-cooling effect. Numerical experiments and scale analysis show that the natural circulation in this first configuration is either one of incomplete vertical penetration, or one of incomplete horizontal penetration. Scale analysis shows that the heat transfer and fluid flow scales differ substantially from one type of penetrative convection to the other, in agreement with the trends revealed by numerical simulations. When the heated portion of the side wall is located below the cooled portion, the flow spreads throughout the porous medium. Scale analysis shows that if the Rayleigh number is sufficiently high, the two mirror-image cells of this flow make contact with the vertical side wall and with each other via slender boundary layer regions. The parametric domain in which the conclusions of this study are valid is outlined on the H/L–Ra_H plane, where H/L is the height/length ratio and Ra_H is the Darcy-modified Rayleigh number based on porous system height.

INTRODUCTION

THE OBJECT of this paper is to draw attention to a relatively unknown class of natural convection flows in porous media, namely, the flows caused by heating and cooling a confined medium along the same vertical wall (Fig. 1). From a practical standpoint, this class of flows is relevant to understanding the functioning of porous insulations exposed to differential heating conditions on one side. From the point of view of basic research in natural convection, this class of flows constitutes an interesting departure from the classical picture painted by the majority of fundamental studies of porous medium convective heat transfer.

Much of the literature devoted to fluid-saturated porous media heated from the side, refers to the case where a temperature difference is maintained between the two vertical walls of the system [1, 2]. The heat and fluid flow characteristics of this case of natural convection are well known: of interest is the fact that this type of natural circulation fills the entire porous layer, i.e. the convection cell is as tall and wide as the layer itself. In this paper we show that when the side wall is differentially heated (Fig. 1), under some circumstances the natural circulation does not occupy the entire porous layer. This example of 'penetrative convection' departs fundamentally from the classical phenomenon reviewed in refs. [1, 2], because penetrative flows have their own (natural) length scales that, in general, differ from the dimensions of the medium in which they develop [3–5]. In this paper we show also that, under a different set of circumstances, the flow spreads throughout the entire system. Thus, the study of natural convection in the configuration sketched in Fig. 1 offers the unique opportunity to encounter a series of fundamentally different flows, a series where one type of penetrative flow may evolve into a different type of penetrative flow or into one that fills the entire porous space.

MATHEMATICAL FORMULATION

The geometry of the porous system of interest is shown in Fig. 1. Three of the four impermeable boundaries are insulated, while the fourth the left wall—is differentially heated. In the first part of the study we consider the case where the upper half of the left wall is heated, as shown in Fig. 1. The opposite case, where the heated region occupies the lower half of the left side wall, is discussed later in this paper. For the temperature distribution along the differentially heated side wall we used the step function

$$T(0,y)-T_0=\begin{cases}-\Delta T, & 0<y<H/2\\ \Delta T, & H/2<y<H\end{cases} \tag{1}$$

where the reference temperature T_0 is the average temperature at midheight, $y = H/2$.

According to the homogeneous porous medium model [1], the equations governing the conservation of mass, momentum and energy in the porous space of Fig. 1 are

$$\frac{\partial u}{\partial x}+\frac{\partial v}{\partial y}=0 \tag{2}$$

NOMENCLATURE

c_p	fluid specific heat at constant pressure
g	gravitational acceleration
H	height of porous layer
k	thermal conductivity of fluid-saturated porous medium
K	permeability
l_x	horizontal penetration distance, Fig. 5(b)
l_y	vertical penetration distance, Fig. 5(a)
L	horizontal dimension of porous layer
m	number of vertical grid lines
n	number of horizontal grid lines
Nu	Nusselt number, equation (17)
P	pressure
Q	overall heat transfer rate
Ra_H	Darcy-modified Rayleigh number based on H, equation (14)
T	temperature
T_0	average temperature
ΔT	temperature step
x	horizontal position
y	vertical position.

Greek symbols

α	thermal diffusivity of homogeneous porous layer
β	coefficient of thermal expansion
δ	vertical boundary layer thickness, Fig. 5
δ_1, δ_2	boundary layer thicknesses defined in Fig. 8
θ	core temperature scale, Fig. 8
μ	viscosity
ν	kinematic viscosity
ρ	density
$\hat{\psi}$	dimensionless streamfunction, equation (10).
$\hat{()}$	dimensionless variables of numerical solutions.

$$u = -\frac{K}{\mu}\frac{\partial P}{\partial x} \tag{3}$$

$$v = -\frac{K}{\mu}\left(\frac{\partial P}{\partial y} + \rho g\right) \tag{4}$$

$$u\frac{\partial T}{\partial x} + v\frac{\partial T}{\partial y} = \alpha\left(\frac{\partial^2 T}{\partial x^2} + \frac{\partial^2 T}{\partial y^2}\right). \tag{5}$$

In these equations, T, P, u, v, and μ are the temperature, pressure, volume-averaged velocity components, and fluid viscosity, respectively. The effective thermal diffusivity of the fluid-saturated porous medium, α, is the ratio $k/(\rho c_p)_f$, where k is the thermal conductivity of the porous medium filled with fluid, and $(\rho c_p)_f$ refers to the heat capacity of the fluid. The two momentum equations, equations (3) and (4), are based on the Darcy flow model in which K represents the permeability of the porous matrix. The model further assumes local thermal equilibrium between the fluid filling the pores and the neighboring solid material.

Eliminating the pressure terms between equations (3) and (4), and invoking the Boussinessq approximation

$$\rho \cong \rho_0[1 - \beta(T - T_0)] \tag{6}$$

yields a single momentum equation that effects the coupling between the temperature field and the flow field

$$\frac{\partial u}{\partial y} - \frac{\partial v}{\partial x} = -\frac{Kg\beta}{\nu}\frac{\partial T}{\partial x}. \tag{7}$$

Relative to the Cartesian system of coordinates shown in Fig. 1, the appropriate boundary conditions for solving equations (2), (5) and (7) are

$u = 0$, $T =$ function given by equation (1), at $x = 0$

$u = 0$, $\dfrac{\partial T}{\partial x} = 0$, at $x = L$

$v = 0$, $\dfrac{\partial T}{\partial y} = 0$, at $y = 0$ and $y = H$. (8)

In the next two sections we rely on direct numerical solutions and on scale analysis to determine the basic features of the natural convection phenomenon taking place in a porous layer heated and cooled from the side.

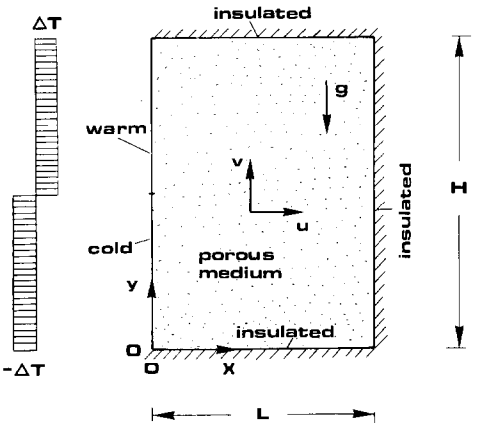

FIG. 1. Two-dimensional porous layer heated and cooled from one side, where the heating region is located above the cooling region.

NUMERICAL SOLUTION

Selecting $H, \alpha/H$ and ΔT as reference units for length, velocity and temperature changes, we place the problem in dimensionless form by defining the new set

of variables

$$\hat{x} = \frac{x}{H}, \quad \hat{y} = \frac{y}{H}$$

$$\hat{u} = \frac{u}{\alpha/H}, \quad \hat{v} = \frac{v}{\alpha/H}$$

$$\hat{T} = \frac{T - T_0}{\Delta T}. \tag{9}$$

Introducing the dimensionless streamfunction $\hat{\psi}$

$$\hat{u} = \frac{\partial \hat{\psi}}{\partial \hat{y}}, \quad \hat{v} = -\frac{\partial \hat{\psi}}{\partial \hat{x}} \tag{10}$$

the governing equations and boundary conditions, equations (2), (5), (7) and (8), assume the new form

$$\frac{\partial^2 \hat{\psi}}{\partial \hat{x}^2} + \frac{\partial^2 \hat{\psi}}{\partial \hat{y}^2} = -Ra_H \frac{\partial \hat{T}}{\partial \hat{x}} \tag{11}$$

$$\frac{\partial}{\partial \hat{x}}(\hat{u}\hat{T}) + \frac{\partial}{\partial \hat{y}}(\hat{v}\hat{T}) = \frac{\partial^2 \hat{T}}{\partial \hat{x}^2} + \frac{\partial^2 \hat{T}}{\partial \hat{y}^2} \tag{12}$$

at $\hat{x} = 0$: $\hat{u} = 0$, $\hat{\psi} = 0$,

$$\hat{T} = -1 \quad \text{for} \quad 0 < \hat{y} < \frac{1}{2}$$

$$\hat{T} = 1 \quad \text{for} \quad \frac{1}{2} < \hat{y} < 1$$

at $\hat{x} = \frac{L}{H}$: $\hat{u} = 0$, $\hat{\psi} = 0$, $\frac{\partial \hat{T}}{\partial \hat{x}} = 0$

at $\hat{y} = 0, 1$: $\hat{v} = 0$, $\hat{\psi} = 0$, $\frac{\partial \hat{T}}{\partial \hat{y}} = 0$ (13)

where Ra_H is the Darcy-modified Rayleigh number based on system height

$$Ra_H = \frac{Kg\beta H \Delta T}{\alpha \nu}. \tag{14}$$

The above formulation shows that the dimensionless solution depends on two dimensionless groups, the Rayleigh number and the aspect or slenderness ratio L/H.

The energy equation (12) was solved using an unconditionally stable finite-difference scheme first proposed by Allen and Southwell [6]. The same scheme was later improved and tested successfully against a number of other finite-difference schemes by Chow and Tien [7]. The Allen–Southwell scheme is an exponential method; its detailed formulation is omitted here, as it can be found in refs. [6, 7]. The streamfunction field was obtained by solving the momentum equation (11), using the successive overrelaxation method [8, 9] and a known temperature distribution.

The rectangular domain of height 1 and thickness (length) L/H was covered with m vertical and n horizontal grid lines. The grid was uniform and, as expected, the necessary number of grid lines depended on Ra_H and L/H. For example, in the case of $Ra_H = 500$ and $H/L = 6$, we found that the grid ($m = 21$, $n = 121$) yielded sufficiently accurate results. The grids used in other cases are listed in Table 1. In cases where we tried to simulate natural convection near a heated and cooled wall facing a semi-infinite medium, $H/L \ll 1$, we used the minimum number of horizontal grid lines that led to a solution satisfying the far-field boundary conditions, $\hat{\psi} = 0$ and $\partial \hat{T}/\partial \hat{x} = 0$, within a prescribed error. Table 1 shows that the largest number of vertical grid lines used was $m = 161$ for the case $Ra_H = 1000$, $H/L = 1/8$. As an additional check on the numerical simulations in the shallow-layer limit, $H/L \ll 1$, we calculated the values of $\hat{T}$ at the insulated end ($x = L/H$) and found that $\hat{T}$ is practically zero (to the sixth decimal point). Therefore, despite the fact that the domain of the numerical solution was finite in length, in order to simulate convection in the $H/L \to 0$ limit we used a long enough domain so that the fluid situated far from the driving wall remained unaffected by the heating and cooling effects provided by the driving wall (for more on this, see the scaling laws of horizontal penetration).

The numerical solutions for the temperature and streamfunction fields resulted from an iterative process repeated until the following convergence criterion was satisfied

$$\frac{\sum_{i=1}^{m}\sum_{j=1}^{n} |\phi_{i,j}^{r+1} - \phi_{i,j}^{r}|}{\sum_{i=1}^{m}\sum_{j=1}^{n} |\phi_{i,j}^{r+1}|} < 10^{-5}. \tag{15}$$

Table 1. Numerical results for natural convection heat transfer in the porous layer configuration of Fig. 1

H/L	Ra_H	Nu	$\hat{\psi}_{min}, \hat{\psi}_{max}$	Grid ($m \times n$)
6	10	2.842	∓0.08	21 × 121
6	20	2.849	∓0.12	21 × 121
6	30	2.855	∓0.17	21 × 121
6	50	2.87	∓0.36	21 × 121
6	70	2.887	∓0.481	21 × 121
6	100	2.916	∓0.646	21 × 121
6	200	3.018	∓1.086	21 × 121
6	300	3.12	∓1.434	21 × 121
6	500	3.303	∓1.964	21 × 121
6	700	3.458	∓2.387	21 × 121
4	500	3.417	∓2.469	21 × 81
2	500	3.688	∓3.523	21 × 41
1	500	3.92	∓4.779	21 × 21
1/2	500	3.093		25 × 13
1/2	500	3.723		33 × 17
1/2	500	4.183		41 × 21
1/2	500	4.2		65 × 33
1/4	10	2.255	∓0.306	81 × 21
1/4	20	2.305	∓0.581	81 × 21
1/4	500	4.245	∓5.785	81 × 21
1/5	30	2.366	∓0.827	101 × 21
1/5	50	2.5	∓1.25	101 × 21
1/5	70	2.639	∓1.61	101 × 21
1/6	100	2.837	∓2.07	121 × 21
1/6	200	3.383	∓3.286	121 × 21
1/6	300	3.775	∓4.232	121 × 21
1/7	500	4.254	∓5.795	141 × 21
1/7	700	4.512	∓7.474	141 × 21
1/8	500	4.254	∓5.795	161 × 21
1/8	1000	4.707	∓9.921	161 × 21

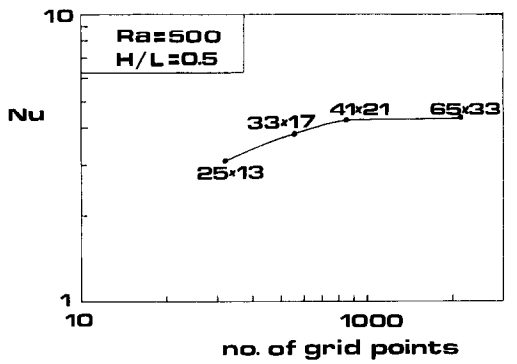

FIG. 2. The relationship between numerical accuracy and grid fineness.

In the above criterion ϕ stands for either $\hat{T}$ or $\hat{\psi}$, and r denotes the iteration cycle.

An important overall parameter that describes the intensity of the natural circulation generated inside the porous system is the net heat transfer rate entering the system through the heated portion of the left wall

$$Q = -k\int_{H/2}^{H}\left(\frac{\partial T}{\partial x}\right)_{x=0} dy. \tag{16}$$

This calculation was cast in dimensionless form as a Nusselt number

$$Nu = \frac{Q}{k\Delta T} = -\int_{1/2}^{1}\left(\frac{\partial \hat{T}}{\partial \hat{x}}\right)_{\hat{x}=0} d\hat{y}. \tag{17}$$

The numerical integration of equation (17) was performed in each (Ra_H, H/L) case, after the final temperature field was reached. From an overall energy conservation perspective, the Nusselt number, equation (17), can also be evaluated based on the heat transfer leaving the system through the cooled portion of the left wall of Fig. 1

$$Nu = \int_{0}^{1/2}\left(\frac{\partial \hat{T}}{\partial \hat{x}}\right)_{\hat{x}=0} d\hat{y}. \tag{18}$$

This second calculation was carried out in each case, in order to check the accuracy of the original Nu estimate, equation (17). Throughout this study the agreement between the two Nusselt number calculations, equations (17) and (18), was better than 1.5%.

The overall Nusselt number was also used to develop an understanding of what grid fineness is needed for sufficiently accurate numerical simulations. As shown in Fig. 2 and Table 1, in the case $Ra_H = 500$, $H/L = 1/2$ a grid containing 41 vertical lines and 21 horizontal lines leads to practically the same Nusselt number as does a grid with more than twice as many grid points (65 × 33). Note that the fineness of the grids used throughout this study, Table 1, is comparable with the fineness of the 41 × 21 whose adequacy is shown in Fig. 2.

VERTICAL PENETRATION vs HORIZONTAL PENETRATION

The main features of the natural convection pattern in a porous layer heated and cooled from one side are shown in Figs. 3 and 4. These figures show both the effect of changing the Rayleigh number Ra_H and the effect of changing the slenderness ratio H/L.

In relatively tall layers, Figs. 3(a) and (b), the effect of increasing the slenderness ratio H/L while keeping Ra_H constant is to snuff out the flow. Note that in going from left to right in Fig. 3(a), the strength of each cell (i.e. $\hat{\psi}_{max}$) decreases (see also Table 1). The flow consists of two cells rotating symmetrically about the horizontal plane positioned at midheight ($y = H/2$). The upper cell is driven clockwise both by the heating effect felt along the left wall and by the cooling effect provided by thermal contact with the lower cell.

The isotherms of Fig. 3(b) show very clearly that as the slenderness ratio H/L becomes large, the upper and lower extremities of the layer fill with relatively stagnant ('trapped') isothermal fluid. The upper end of the $H/L = 6$ system, for example, is saturated with fluid as hot as the heated section of the left wall: this fluid is unable to feel the cooling effect available near the $y = H/2$ plane, and remains trapped at the highest altitude possible. The same is true for the cold fluid saturating the $y = 0$ end of the slender tall layer.

In relatively shallow layers, Figs. 4(a) and (b), the flow again consists of two mirror-image cells driven by the left wall. Each cell is $H/2$ high; the length of each cell, however, depends on the Rayleigh number in such a way that the higher the Ra_H the longer the x-distance to which the fluid travels before being sucked back into the left wall boundary layer. If the layer is longer than the natural horizontal penetration length of each cell, then the right end of the layer fills with relatively motionless isothermal fluid that does not participate in the convection heat exchange between the differentially-heated portions of the left wall. In each of the cases shown in Figs. 4(a) and (b) the right half of the layer ($L/2 < x < L$) is not shown because it is occupied by relatively inactive fluid. The flow patterns of Figs. 4(a) and (b) do not change in a significant way if L increases while H and Ra_H are held fixed: in each case, the relatively inactive region located near the right end increases in length as L increases, leaving the penetrative flow driven by the $x = 0$ end unchanged.

To summarize, the message of Figs. 3 and 4 is that the natural convection pattern is in some cases one of incomplete 'vertical penetration', as in the last two cases of Fig. 3, while in other cases the pattern may be characterized as one of incomplete 'horizontal penetration' (Fig. 4). As shown later in this study, these two distinct manifestations of the natural convection phenomenon are accompanied by distinct scaling laws that govern the overall heat transfer between the differentially heated portions of the left wall. In the next two sections we rely on scale analysis to predict the flow features and trends revealed by the numerical simulations shown in Figs. 3 and 4.

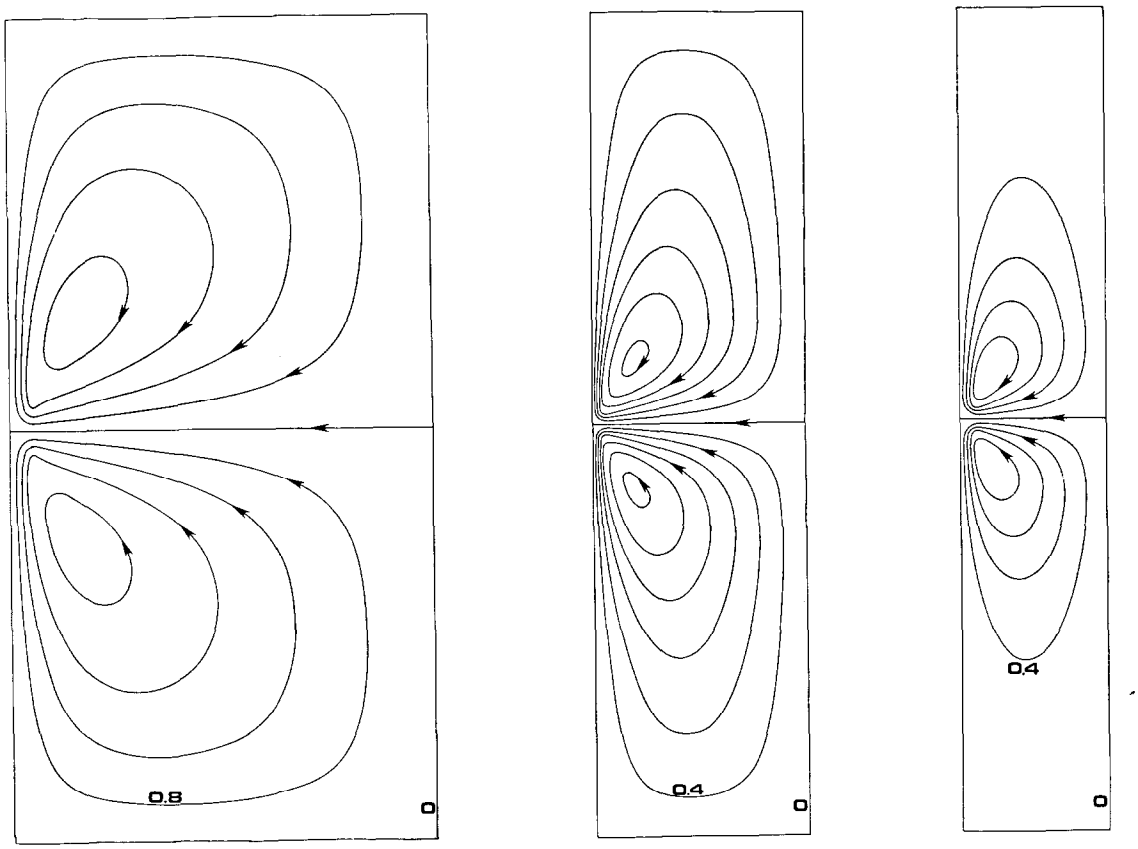

(a)

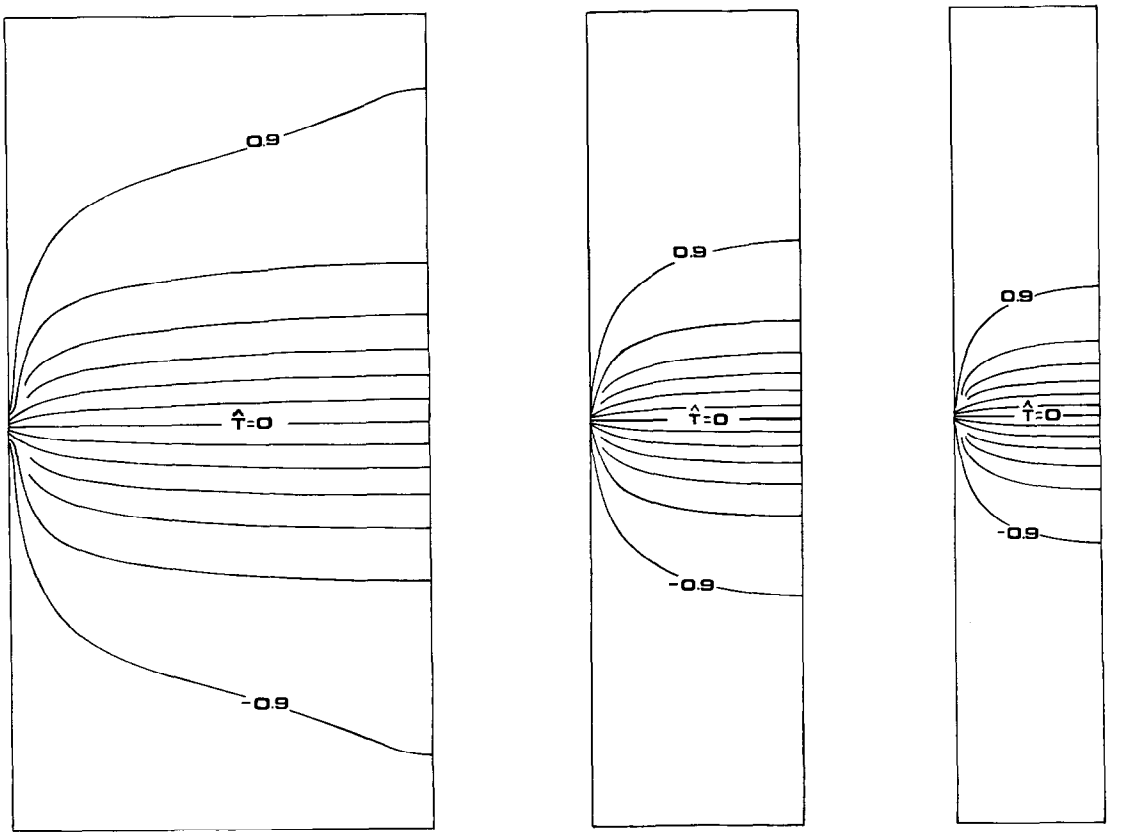

(b)

FIG. 3. Numerical results for $Ra_H = 500$ and $H/L = 2, 4, 6$, showing the incomplete vertical penetration: (a) streamlines; (b) isotherms.

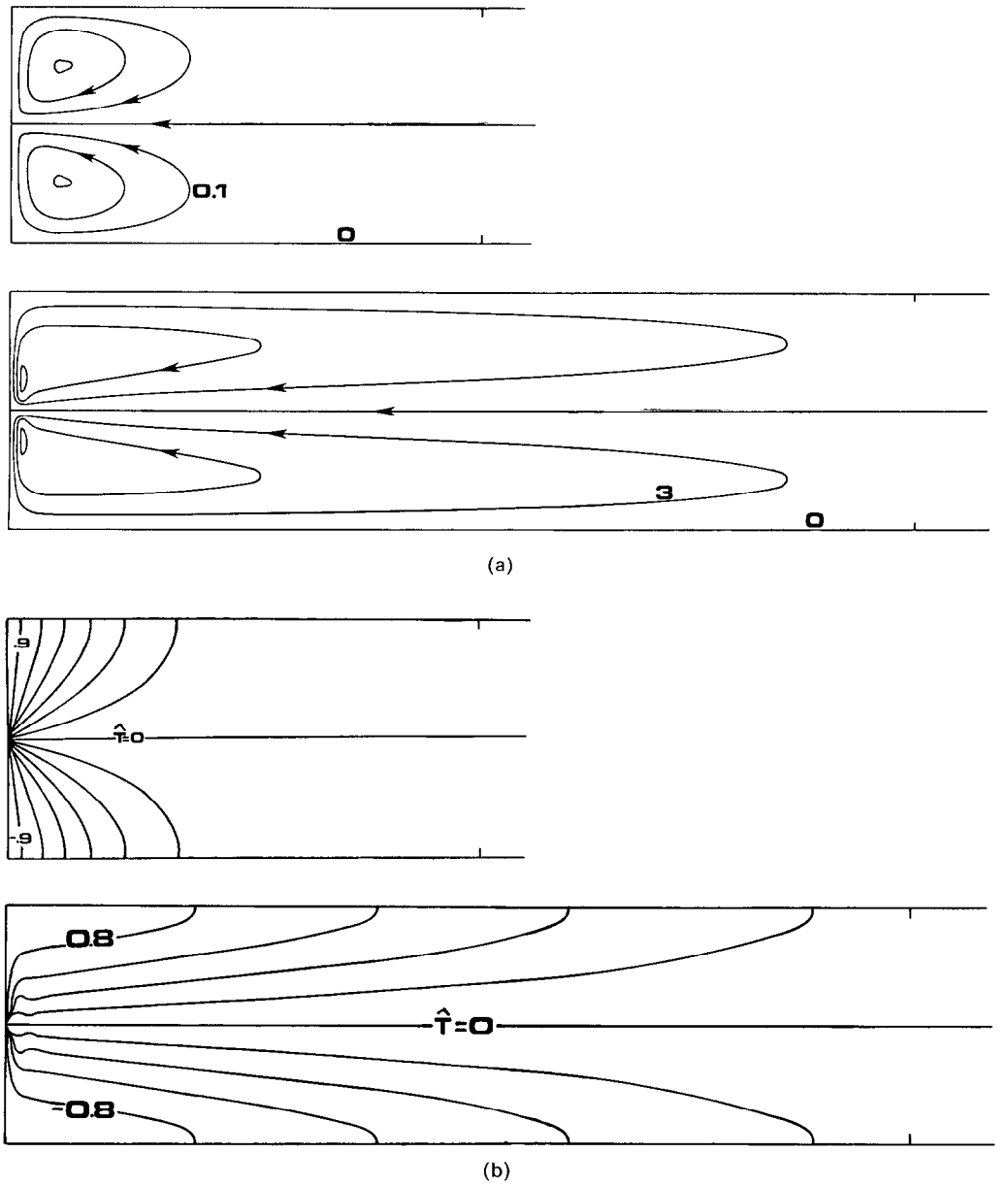

FIG. 4. Numerical results showing the phenomenon of incomplete horizontal pentration (top: $Ra_H = 10$, $H/L = 1/4$; bottom: $Ra_H = 1000$, $H/L = 1/8$): (a) streamlines; (b) isotherms.

THE SCALING LAWS OF VERTICAL PENETRATION

As shown in Fig. 5(a), let us assume that each cell is shorter than the maximum height to which it could spread vertically

$$l_y \ll H/2. \tag{19}$$

We further assume that the cellular flow makes thermal contact with the vertical heated wall through a slender vertical region, i.e. through a boundary layer

$$\delta \ll l_y. \tag{20}$$

In the boundary layer region whose height is l_y and thickness δ, the momentum and energy equations (7) and (5) require the following balances of scales

$$\text{(momentum)} \quad \frac{v}{\delta} \sim \frac{Kg\beta}{\nu}\frac{\Delta T}{\delta} \tag{21}$$

$$\text{(energy)} \quad v\frac{\Delta T}{l_y} \sim \alpha\frac{\Delta T}{\delta^2}. \tag{22}$$

In addition, the heat transfer rate from the left wall to the vertical boundary layer [Q, equation (16)] must be the same as the thermal diffusion rate downward through the plane separating the two cells

$$Q \sim kl_y\frac{\Delta T}{\delta} \sim kL\frac{\Delta T}{l_y}. \tag{23}$$

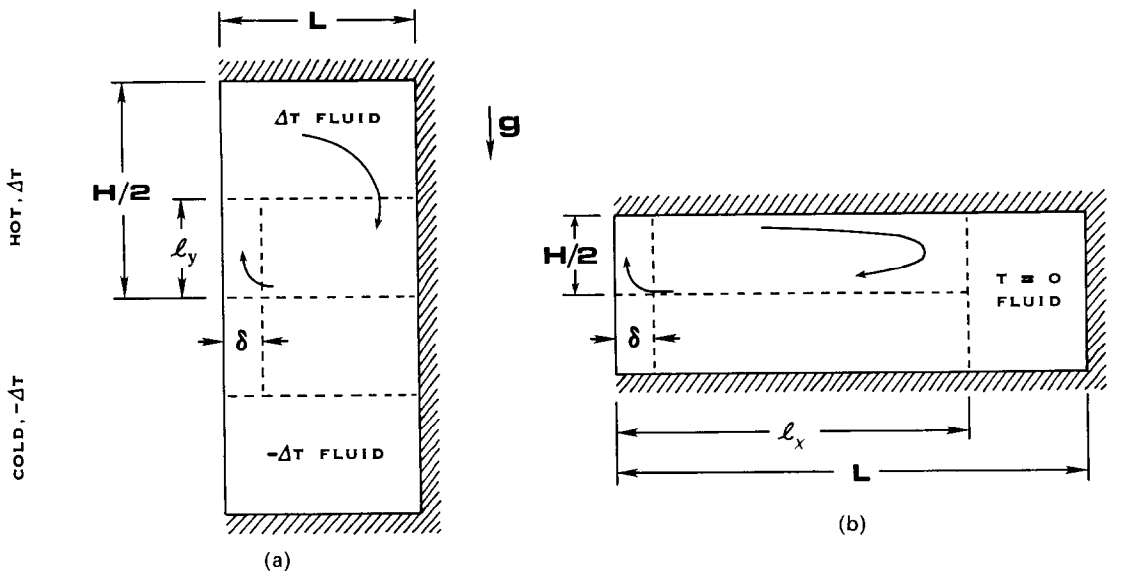

FIG. 5. The scales of natural convection in the configuration of Fig. 1 : (a) incomplete vertical penetration ; (b) incomplete horizontal penetration.

Equations (21)–(23) are sufficient for determining the unknown scales of the cellular flow of Fig. 5(a), in particular the geometry of the vertical boundary layer

$$l_y/H \sim Ra_H^{-1/3}\left(\frac{L}{H}\right)^{2/3} \tag{24}$$

$$\delta \sim L\left(Ra_H \frac{L}{H}\right)^{-2/3}. \tag{25}$$

Equation (24) shows that when Ra_H is fixed, the vertical penetration distance l_y/H decreases as the slenderness ratio H/L increases. The same trend is exhibited by the numerical solutions plotted in Fig. 3. The dimensionless streamfunction scale corresponding to the conservation statements, equation (21)–(23), is

$$\hat{\psi} \sim \hat{v}\hat{x} \sim \frac{v}{\alpha/H}\frac{\delta}{H} \sim \left(Ra_H \frac{L}{H}\right)^{1/3}. \tag{26}$$

Thus, the $\hat{\psi}$ scale must decrease if H/L increases and if Ra_H is held constant: this conclusion is also in agreement with the numerical results of Fig. 3. Finally, the Nusselt number defined by equation (17) is of the order of

$$Nu \sim \frac{l_y}{\delta} \sim \left(Ra_H \frac{L}{H}\right)^{1/3}. \tag{27}$$

In a layer with H/L fixed, in the convection-dominated regime the Nusselt number must vary as $Ra_H^{1/3}$: this conclusion is supported by the $H/L = 6$ data displayed in Fig. 6, which—despite the still dominant effect of

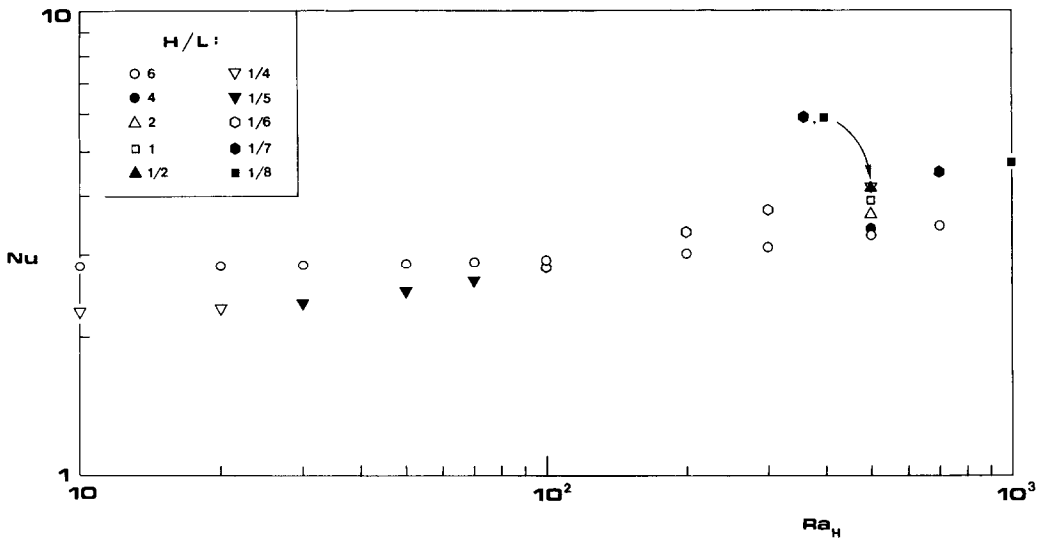

FIG. 6. Numerical results for the overall heat transfer rate through the system of Fig. 1.

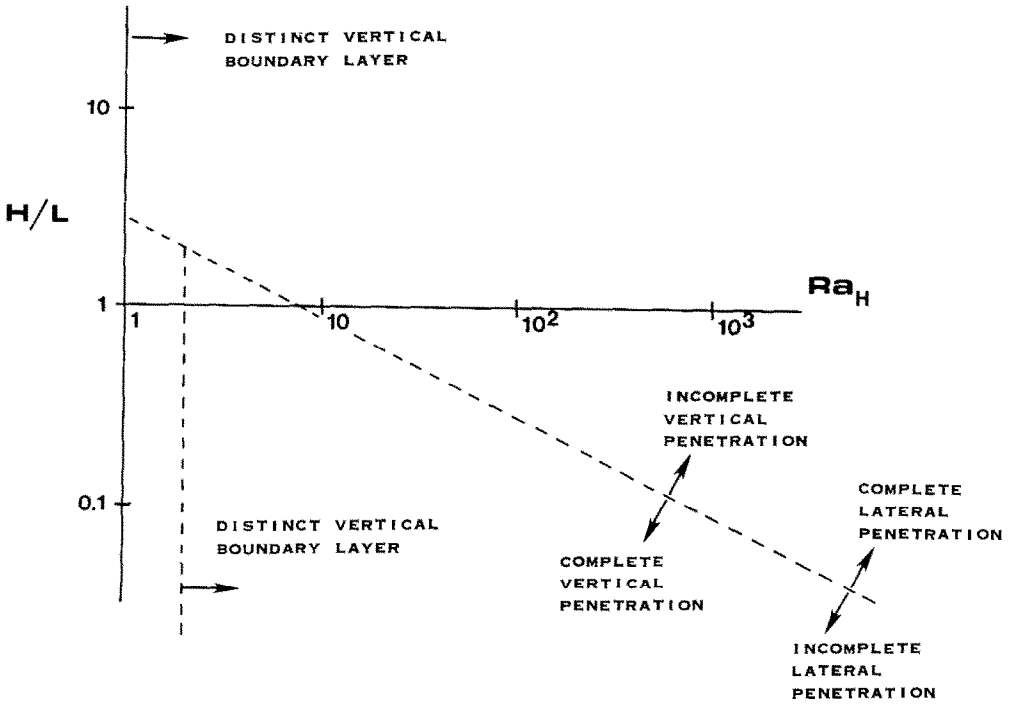

FIG. 7. The locus of the phenomena of incomplete vertical penetration and incomplete horizontal penetration, on the H/L–Ra_H plane.

conduction—shows that Nu increases slower than $Ra_H^{1/2}$.

The domain of validity of results (24)–(27) was defined in the beginning of the scale analysis via conditions (19) and (20). These conditions can be rewritten as

$$\frac{H}{L} Ra_H^{1/2} \gg 2^{3/2} \tag{28}$$

$$\frac{L}{H} Ra_H \gg 1, \tag{29}$$

where equation (28) represents the condition necessary for incomplete vertical penetration, equation (19), and where equation (29) represents the condition for boundary layer convection, equation (20). Figure 7 shows the ways in which conditions (28) and (29) divide the H/L–Ra_H domain.

THE SCALING LAWS OF HORIZONTAL PENETRATION

Consider the situation sketched in Fig. 5(b), where the distance of horizontal penetration l_x is shorter than the horizontal dimension of the porous layer

$$l_x \ll L. \tag{30}$$

If, in addition, the boundary layer region coating the vertical wall is slender

$$\delta \ll H/2 \tag{31}$$

then, from equations (7) and (5), in the region of height $H/2$ and thickness δ we have the following equivalences of scales

$$\text{(momentum)} \quad \frac{v}{\delta} \sim \frac{Kg\beta\Delta T}{\nu} \frac{\delta}{} \tag{32}$$

$$\text{(energy)} \quad v\frac{\Delta T}{H/2} \sim \alpha \frac{\Delta T}{\delta^2}. \tag{33}$$

Combining equations (32) and (33), we find

$$\delta \sim 2^{-1/2} H\, Ra_H^{-1/2}. \tag{34}$$

Alone, the vertical boundary layer scaling, equation (32)–(34), dictates the flow rate of the cellular flow and the heat transfer extracted by the flow from the vertical wall

$$\hat{\psi} \sim \frac{v\delta}{\alpha} \sim 2^{-1/2}\, Ra_H^{1/2} \tag{35}$$

$$Nu \sim \frac{Q}{k\Delta T} \sim \frac{H}{2\delta} \sim 2^{-1/2}\, Ra_H^{1/2}. \tag{36}$$

These laws are validated by Table 1 and Fig. 6, which show that in shallow layers at high Rayleigh numbers the values of Nu and $\hat{\psi}_{max}$ are practically independent of the slenderness ratio H/L.

The conservation of momentum and energy in the slender region of length l_x and height $H/2$, Fig. 5(b), requires

$$\text{(momentum)} \quad \frac{u}{H/2} \sim \frac{Kg\beta}{\nu} \frac{\Delta T}{l_x} \tag{37}$$

$$\text{(energy)} \quad u\frac{\Delta T}{l_x} \sim \alpha \frac{\Delta T}{(H/2)^2}. \tag{38}$$

Eliminating u between equations (37) and (38) yields the scale of the horizontal penetration distance

$$l_x \sim 2^{-3/2} H\, Ra_H^{1/2}. \tag{39}$$

The above conclusion—the increase in horizontal penetration with $Ra_H^{1/2}$—is verified qualitatively by the flow patterns plotted in Fig. 4(a).

The domain of validity of the scale analysis constructed in this section is determined by rewriting the two starting conditions, equations (30) and (31), as

$$\frac{H}{L} Ra_H^{1/2} \ll 2^{3/2} \tag{40}$$

$$Ra_H \gg 2. \tag{41}$$

The frontiers of this domain are also sketched in Fig. 7. Note that criteria (28) and (40) are mutually exclusive: this means that in a layer with $H/L < 1$ and fixed, and with increasing Ra_H, as soon as the horizontal penetration becomes complete ($l_x \gtrsim L$) the vertical penetration becomes incomplete ($l_y \lesssim H/2$). In other words, the cellular flow fills the entire porous space available to it only in the special case

$$\frac{H}{L} Ra_H^{1/2} \sim 2^{3/2}. \tag{42}$$

SIDE HEATING POSITIONED BELOW SIDE COOLING

The preceding numerical solutions and scale analyses all focused on the arrangement shown in Fig. 1, where the porous layer is heated and cooled from the side in such a way that the heating effect is positioned above the cooling effect. In this section we consider the reverse situation where the heated section of the side wall is located below the cooled section (Fig. 8). This situation is simpler (less ambiguous) than the one analyzed so far, because the 'incomplete penetration' phenomenon is no longer a feature of high Rayleigh number convection. As shown by numerical simulations and scale analysis, the flow consists of two cells of height $H/2$ and length L; in other words, each cell fills the maximum space available.

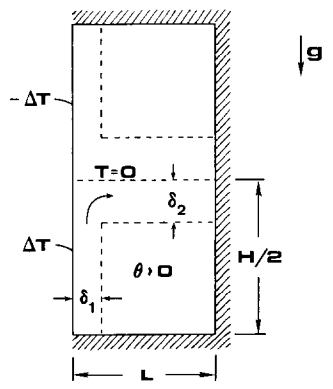

FIG. 8. The scales of natural convection in a system with the effect of side cooling positioned above the effect of side heating.

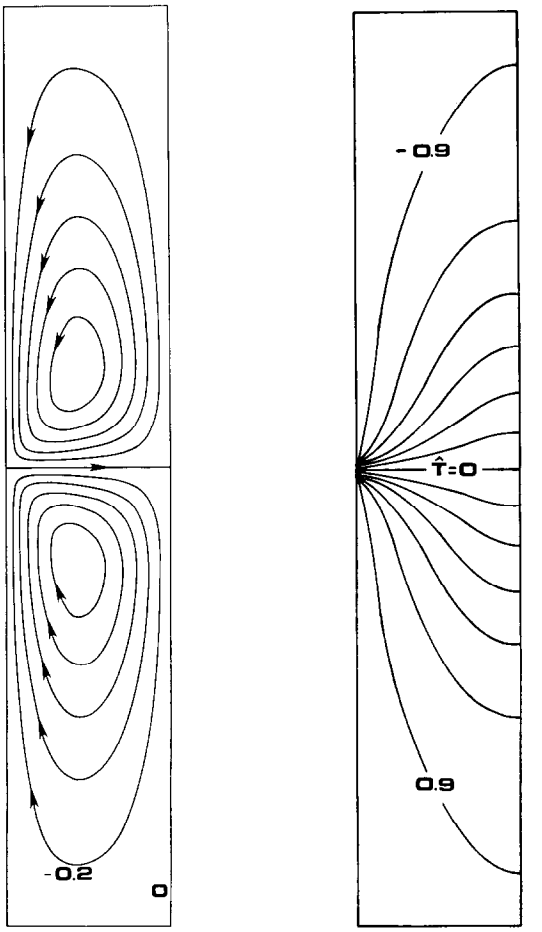

FIG. 9. Streamlines and isotherms for the case $Ra_H = 100, H/L = 6$, in a system with the effect of side cooling located above the effect of side heating.

Figure 9 shows a sample numerical solution for a relatively tall layer, $H/L = 6$, at a relatively low Rayleigh number, $Ra_H = 100$. Focusing on the lower of the two cells, we see that even at this Rayleigh number the circulation consists of two boundary layers connected through a slower moving core. One boundary layer coats the hot vertical wall section of temperature ΔT, while the other layer is actually a horizontal jet of centerline temperature $T = 0$. Provided the Rayleigh number is high enough, the existence of these two slender regions ($\delta_1 \times H/2$ and $\delta_2 \times L$ on Fig. 8) is not likely to be threatened by changes in the aspect ratio H/L; since the heated wall section is located below the cooled section, the cooler core fluid ($T \sim \theta$, Fig. 8) must sweep the entire height of the hot wall section ($H/2$), and, once at the top, the heated stream can only spread horizontally as far as it can go, i.e. to $x \sim L$. For this reason, the flow triggered by the arrangement of Fig. 8 is not one of 'penetrative convection' because the outer dimensions of the cell always coincide with the dimensions of the porous system itself, $H/2$ and L.

Much of the qualitative discussion made possible by numerical experiments of the type exhibited in Fig. 9,

can be backed by scale analysis. The starting point in the scale analysis is that the two boundary layers of the lower cell in Fig. 8 are slender

$$\delta_1 \ll H/2 \tag{43}$$

$$\delta_2 \ll L, \quad \delta_1 \neq \delta_2. \tag{44,45}$$

The domain of validity of these assumptions will become clear at the end of the scale analysis, when the δ_1, δ_2 scales are known. In the vertical boundary layer region of height $H/2$ and thickness δ_1, we account for momentum and energy conservation by writing

$$\text{(momentum)} \quad \frac{v}{\delta_1} \sim \frac{Kg\beta}{\nu}\frac{\Delta T-\theta}{\delta_1} \tag{46}$$

$$\text{(energy)} \quad v\frac{\Delta T-\theta}{H/2} \sim \alpha\frac{\Delta T-\theta}{\delta_1^2}. \tag{47}$$

Here, the temperature scale θ is the intermediate temperature acquired by the core region (Fig. 8), $\Delta T > \theta > 0$. Eliminating v between equations (46) and (47) yields the thickness of the vertical boundary layer

$$\delta_1 \sim \left[\frac{\alpha\nu H}{2Kg\beta(\Delta T-\theta)}\right]^{1/2} \tag{48}$$

which shows that the problem is not solved until the core temperature θ is determined.

Turning our attention to the horizontal jet region of length L and thickness δ_2 (see Fig. 8), the governing equations (7) and (5) require

$$\text{(momentum)} \quad \frac{u}{\delta_2} \sim \frac{Kg\beta}{\nu}\frac{\Delta T-\theta}{L} \tag{49}$$

$$\text{(energy)} \quad u\frac{\Delta T-\theta}{L} \sim \alpha\frac{\theta}{\delta_2^2}. \tag{50}$$

Combining equations (49) and (50) we find the thickness of the horizontal jet

$$\delta_2 \sim \left[\frac{\alpha\nu L^2\theta}{Kg\beta(\Delta T-\theta)^2}\right]^{1/3} \tag{51}$$

which also depends on the unknown temperature of the core, θ.

The problem is finally closed by 'matching' the two boundary layers: writing that the heat transfer rate extracted by the vertical boundary layer from the ΔT wall must equal the heat transfer rate to the upper (colder) cell, we have

$$Q \sim k\frac{H}{2}\frac{\Delta T-\theta}{\delta_1} \sim kL\frac{\theta}{\delta_2}. \tag{52}$$

Substituting into this overall energy balance the (δ_1, δ_2) scales derived already, equations (48) and (51), we obtain the core temperature scale θ; in the dimensionless form, the θ result is

$$\frac{8(\theta/\Delta T)^4}{(1-\theta/\Delta T)^5} \sim Ra_H\left(\frac{H}{L}\right)^2. \tag{53}$$

Note that the same result would follow also from the claim that the two boundary layers handle the same flow rate: $v\delta_1 \sim u\delta_2$: this condition would have to be used in place of equation (52).

According to equation (53), the core temperature scale varies with both Ra_H and H/L through the aggregate group $Ra_H(H/L)^2$. The two limits of this dependence are investigated separately below.

I. $\theta/\Delta T \sim 1$, or, from equation (53)

$$1-\frac{\theta}{\Delta T} \sim 2^{3/5}Ra_H^{-1/5}\left(\frac{H}{L}\right)^{-2/5}. \tag{54}$$

The Nusselt number in this limit scales as

$$Nu = \frac{Q}{k\Delta T} \sim 2^{2/5}Ra_H^{1/5}\left(\frac{H}{L}\right)^{-3/5} \tag{55}$$

while the other scales of interest reduce to

$$\frac{\delta_1}{H} \sim 2^{-4/5}Ra_H^{-2/5}\left(\frac{H}{L}\right)^{1/5} \tag{56}$$

$$\frac{\delta_2}{H} \sim 2^{-2/5}Ra_H^{-1/5}\left(\frac{H}{L}\right)^{-2/5}. \tag{57}$$

Note that the vertical boundary layer thickness δ_1 decreases faster than δ_2 as Ra_H increases.

II. $\theta/\Delta T \ll 1$, or, from equation (53)

$$\frac{\theta}{\Delta T} \sim 2^{-3/4}Ra_H^{1/4}\left(\frac{H}{L}\right)^{1/2}. \tag{58}$$

Neglecting θ at the expense of ΔT whenever θ and ΔT appear in a sum together, the heat transfer and length scales become

$$\frac{\delta_1}{H} \sim 2^{-1/2}Ra_H^{-1/2} \tag{59}$$

$$\frac{\delta_2}{H} \sim 2^{-1/4}Ra_H^{-1/4}\left(\frac{H}{L}\right)^{-1/2} \tag{60}$$

$$Nu \sim 2^{-1/2}Ra_H^{1/2}. \tag{61}$$

Note that, again, δ_1 decreases faster than δ_2 as Ra_H increases. Also, in this limit the Nusselt number scales the same way as in the 'horizontal penetration' regime of the configuration considered during the first part of this study [Fig. 4, equation (36)].

The frontier between limits I and II can be obtained either by setting $\theta/\Delta T \sim 1$ in equation (58), or by equating the Nusselt numbers given by equations (55) and (61); the resulting criterion is

$$\begin{aligned} &\text{I.} \quad Ra_H\left(\frac{H}{L}\right)^2 \gg 8 \\ &\text{II.} \quad Ra_H\left(\frac{H}{L}\right)^2 \ll 8. \end{aligned} \tag{62}$$

The H/L–Ra_H domain in which the above scaling results apply is defined by the boundary layer slenderness conditions, equations (43) and (44), and by two additional conditions stating that both boundary layers are distinct

$$\delta_1 \ll L \tag{63}$$

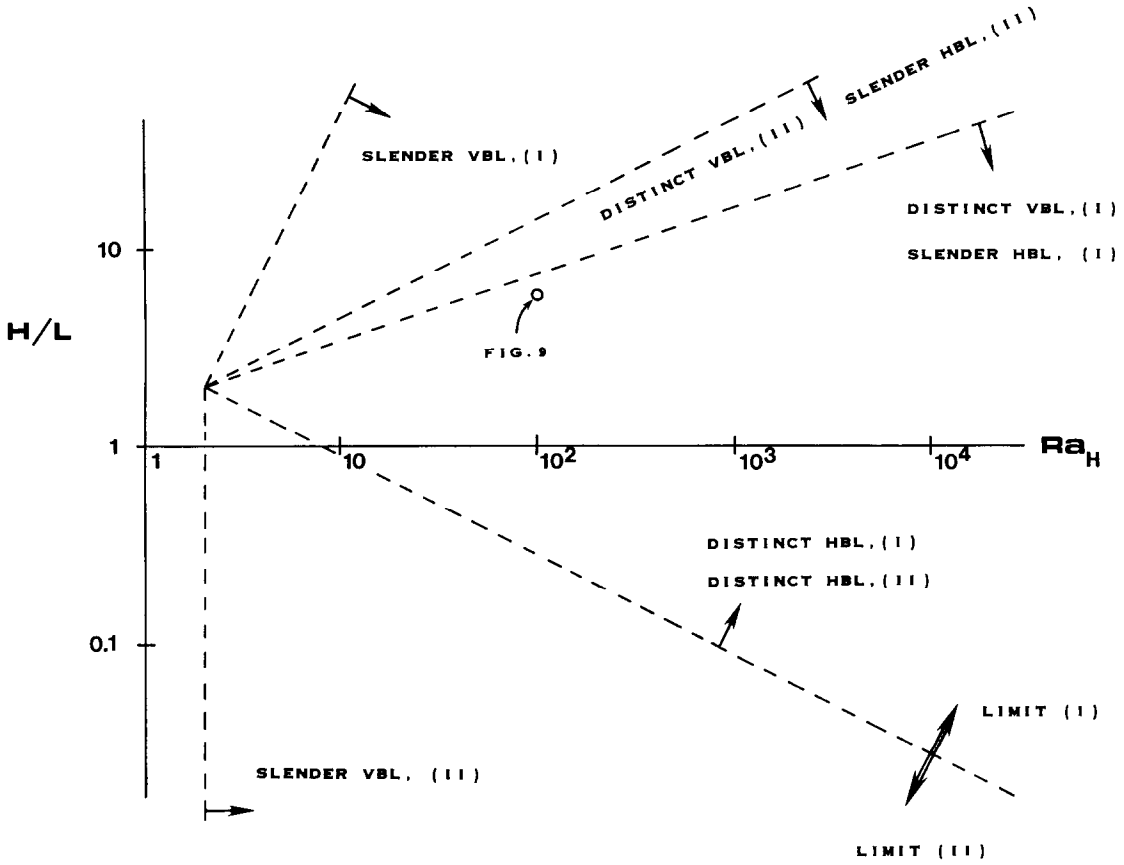

FIG. 10. The domain H/L–Ra_H where the scale analysis based on Fig. 8 is valid.

$$\delta_2 \ll H/2. \tag{64}$$

Given the two limits (I and II) identified in connection with scale of core temperature, the validity conditions, equations (43) and (44) and equations (63) and (64), generate a total of eight inequalities involving H/L and Ra_H. The space limitations faced by this report do not permit the derivation and listing of all these inequalities, some of which are more severe than others. For brevity, they are all shown graphically in Fig. 10: in each case, the arrow indicates the semi-infinite domain in which a particular condition is satisfied (note the abbreviations: VBL, vertical boundary layer; HBL, horizontal boundary layer). The graph shows also the frontier between limits I and II, given by criterion (62).

One important conclusion brought to light by Fig. 10 is that throughout the domain occupied by limit II ($\theta \ll \Delta T$) the horizontal boundary layer is not distinct. Therefore, the scales represented by equations (59)–(61), although useful in determing the I/II frontier, equation (62), and in drawing Fig. 10, do not describe a real flow. These scales can be corrected easily by repeating the scale analysis, using $H/2$ instead of δ_2 as transversal length scale in the horizontal jet (i.e. assuming from the start that the horizontal slender layer is not distinct).

The other conclusion made possible by Fig. 10 is that the limit I results represented by equations (55)–(57) are valid in the innermost wedge-shaped region narrowed down by the eight inequalities generated by equations (43) and (44) and equations (63) and (64). This region is bounded from above by the condition for distinct vertical boundary layer in limit I, and from below by the condition of distinct horizontal boundary layer in limit I; analytically, this wedge-shaped region is

$$2^{2/3}Ra_H^{1/3} \gg \frac{H}{L} \gg 2^{3/2}Ra_H^{-1/2}. \tag{65}$$

In other words, the cellular flow is always characterized by distinct vertical and horizontal side layers (as in Fig. 8) if Ra_H is high enough. However, it should be kept in mind that the arrangement of Fig. 8 is potentially unstable, hence, Ra_H cannot be increased indefinitely without leading to a Bénard-type instability in the slender horizontal jet that separates the upper cold cell from the lower warm cell. The possible high-Ra_H breakdown of the two-cell flow shown in Fig. 9 remains to be researched based on a case-by-case mapping of the wedge-shaped region, equation (65).

CONCLUDING REMARKS

In this study we examined the heat transfer through a porous layer heated and cooled from one side, by

considering first the case when the side-heating effect is positioned above the side-cooling effect (Fig. 1). Numerical experiments and scale analysis showed that the natural convection phenomenon in this first configuration is either one of incomplete vertical penetration [Figs. 3 and 5(a)] or one of incomplete horizontal penetration [Figs. 4 and 5(b)]. It was found that the heat and fluid flow scales differ markedly from one type of penetrative convection to the other, in agreement with the trends revealed by numerical simulations. When the heated portion of the side wall is located under the cooled portion, Figs. 8 and 9, the flow spreads throughout the porous medium. Scale analysis showed that if the Rayleigh number is sufficiently high the two cells make contact with the vertical side wall and with each other via slender boundary layer regions. For both configurations, the parametric domain in which the scale analysis results are valid has been outlined on the H/L–Ra_H plane (Figs. 7 and 10). Overall, the relatively simple geometry of a porous layer heated and cooled from one side can play host to surprisingly diverse penetrative or non-penetrative natural convection flows, depending on H/L, Ra_H, and the relative position of the heating and cooled portions of the side wall.

Acknowledgement—This study was supported by the National Science Foundation, through Grant No. MEA-82-07779.

REFERENCES

1. P. Cheng, Heat transfer in geothermal systems, *Adv. Heat Transfer* **14**, 1–105 (1978).
2. A. Bejan, A synthesis of analytical results for natural convection heat transfer across rectangular enclosures, *Int. J. Heat Mass Transfer* **23**, 723–726 (1980).
3. D. Poulikakos and A. Bejan, Penetrative convection in porous medium bounded by a horizontal wall with hot and cold spots, *Int. J. Heat Mass Transfer* **27**, 1749–1757 (1984).
4. A. Bejan, Natural convection in a vertical cylindrical well filled with porous medium, *Int. J. Heat Mass Transfer* **23**, 726–729 (1980).
5. A. Bejan, Lateral intrusion of natural convection into a horizontal porous structure, *Trans. Am. Soc. Mech. Engrs*, Series C, *J. Heat Transfer* **103**, 237–241 (1981).
6. D. N. de G. Allen and R. V. Southwell, Relaxation methods applied to determine the motion in two dimensions of a viscous fluid past a fixed cylinder, *Q. Jl. Mech. Appl. Math.* **8**, 129–145 (1955).
7. L. C. Chow and C. L. Tien, An examination of four differencing schemes for some elliptic-type convection equations, *Num. Heat Transfer* **1**, 87–100 (1978).
8. P. J. Roache, *Computational Fluid Dynamics*, pp. 117–119. Hermosa, Albuquerque (1976).
9. C. Y. Chow, *An Introduction to Computational Fluid Mechanics*, pp. 160–161. Wiley, New York (1979).

CONVECTION NATURELLE DANS UNE COUCHE POREUSE CHAUFFEE ET REFROIDIE SUR UN COTE VERTICAL

Résumé—On décrit le transfert thermique et l'écoulement à travers une couche poreuse confinée, chauffée et refroidie sur un côté vertical. Dans la première partie, on considère le cas où le chauffage latéral est placé au dessus du refroidissement latéral. Des expériences numériques et une analyse d'échelle montrent que la circulation naturelle dans cette première configuration est soit celle d'une pénétration verticale incomplète, soit celle d'une pénétration horizontale incomplète. L'analyse d'échelle montre que les échelles du transfert thermique et de l'écoulement diffèrent nettement d'un type de pénétration à l'autre, en accord avec les tendances visibles par le calcul numérique. Lorsque la portion chauffée de la paroi est située au dessous de la portion froide, l'écoulement s'étend dans le milieu poreux. L'analyse d'échelle montre que si le nombre de Rayleigh est suffisamment élevé, les deux cellules de cet écoulement sont en contact avec le côté vertical et avec l'autre par l'intermédiaire de régions minces de couche limite. Le domaine paramétrique dans lequel les conclusions de cette étude sont valables est délimité dans le plan H/L–Ra_H, où H/L est le rapport hauteur/longueur et Ra_H est le nombre de Rayleigh modifié selon Darcy et basé sur la hauteur du système poreux.

FREIE KONVEKTION IN EINER PORÖSEN SCHICHT, DIE AN EINER SENKRECHTEN SEITE BEHEIZT UND GEKÜHLT WIRD

Zusammenfassung—Diese Arbeit beschreibt den Wärmetransport und die Fluidströmung durch eine schmale poröse Schicht, die an jeweils einer der senkrechten Seitenwänden beheizt und gekühlt wird. Im ersten Teil der Arbeit wird eine Betrachtung für den Fall angestellt, daß der geheizte Teil der Seite über dem gekühlten Teil angeordnet ist. Numerische Untersuchungen und eine Modellbetrachtung zeigen, daß die natürliche Zirkulation in dieser ersten Anordnung entweder eine unvollständige senkrechte oder eine unvollständige waagerechte Durchdringung darstellt. Modelluntersuchungen zeigen, daß die Wärmetransport- und Fluidströmungsmaßstäbe sich wesentlich von einer Art der Durchdringungskonvektion zur anderen unterscheiden, was in Übereinstimmung mit den Voraussagen steht, die mit Hilfe von numerischen Simulationen erhalten wurden. Wenn der beheizte Teil der Seitenwand unter den gekühlten Teil angeordnet wird, verbreitet sich Strömung durch das gesamte poröse Medium. Ähnlichkeitsbetrachtungen zeigen, daß im Fall von genügend hohen Rayleigh-Zahlen zwei spiegelbildliche Zellen dieser Strömung durch dünne Grenzschichtgebiete mit der senkrechten Seitenwand und miteinander Kontakt haben. Der Parameterbereich, in dem die Ergebnisse dieser Untersuchung gelten, ist gekennzeichnet durch die H/L, Ra_H-Ebene, wobei H/L das Höhen/Längen Verhältnis und Ra_H die Darcy-modifizierte Rayleigh-Zahl ist, die auf die Höhe des porösen Systems bezogen ist.

ЕСТЕСТВЕННАЯ КОНВЕКЦИЯ В ПОРИСТОМ СЛОЕ С НАГРЕВОМ И ОХЛАЖДЕНИЕМ ВДОЛЬ ОДНОЙ ВЕРТИКАЛЬНОЙ СТОРОНЫ

Аннотация Описываются теплообмен и течение жидкости в ограниченном пористом слое, нагреваемом и охлаждаемом вдоль одной из вертикальных стенок. В первой части работы рассматривается случай, когда нагреваемый участок находится выше охлаждаемого. Численные эксперименты и анализ подобия показывают, что в этом случае конвекция недостаточно полно проникает либо в вертикальном, либо в горизонтальном направлении. Из анализа подобия следует, что характерные величины для теплопереноса и течения жидкости для каждого типа проникающей конвекции существенно отличаются друг от друга, что подтверждается также результатами численного моделирования. Когда нагреваемый участок боковой стенки расположен ниже охлаждаемого, конвекция распространяется по всей пористой среде. Из анализа подобия видно, что при довольно большом значении числа Рэлея две зеркально подобные ячейки этого потока контактируют с вертикальной боковой стенкой и друг с другом через тонкие пограничные слои. Область параметров, для которой справедливы полученные в работе выводы, нанесена на плоскости H/L, Ra_H, где H/L — отношение высоты к длине, а Ra_H — Дарси-модификация числа Рэлея, основанного на высоте пористой системы.